ADVANCED OPTICAL MATERIALS
www.advopticalmat.de

Tunable Structural Color with Gradient and Multiaxial Polydimethylsiloxane Wrinkling

*Annabelle Tan, Luca Pellegrino, Zain Ahmad, and João T. Cabral**

The generation of structural color from wrinkled polydimethylsiloxane (PDMS) surfaces, fabricated by plasma exposure, subjected to uni- and multi-axial, and sequential strain fields is examined. The approach is based on the well-known, mechanically-induced, buckling instability of a supported bilayer, whereby the top glassy "skin" is formed by plasma oxidation. Surface periodicities 200 nm $\lesssim d \lesssim$ 3 µm, encompassing the visible spectrum, are investigated in terms of the observed color, intensity spectrum, and color mixing from different diffraction orders, exhibiting good agreement with model predictions. By contrast with complex fabrication methods, color tunability and mechanochromic response are readily achieved by adjusting plasma and strain parameters, and by dynamically varying strain ($\varepsilon \lesssim 50\%$). Prescribed strain directionality, employing uniaxial, isotropic, gradient strain, and wave-sum wrinkling superposition, as well as skin thickness (and thus d) and amplitude gradients, using facile and scalable fabrication approaches, yield striking spatial color variation, homogeneity, and directionality.

1. Introduction

Inspired by the abundance of structural color in nature,[1–7] a range of material synthesis and processing approaches have been developed to design nano- and microstructures, including multilayer films,[8,9] photonic crystals,[10,11] and metasurfaces,[12,13] exhibiting static and variable structural colors, tailored to various practical applications.[14–17] Wrinkled surface structures, found in flowers and insects[18–20] have been shown to act as surface diffraction gratings, imparting structural color to flower petals such as in the queen of the night tulip[21] and the *Hibiscus trionum*,[22] as well as enhancing the diffuse reflection in dragonflies *Rhyothemis resplendens*.[20] Randomly oriented wrinkles were demonstrated to produce uniform bright structural colors with broad viewable angles, which can further be tunable using light sensitive polymers skins.[23]

Mechanochromic response, that is, the change of color under stress, of wrinkled structures has been recently reported, employing various bilayer film structures.[22,24,25] The use of soft matter substrates, including elastomers, is advantageous as it readily allows optical properties to be tuned by the applied strain, by adjusting surface periodicity and amplitude, in addition to film thickness and mechanical modulus. Further, a wide range of surface patterns, including uni- and multiaxial and hierarchical wrinkles, can be readily fabricated. Bilayers are generally fabricated by deposition or lamination of a thin and stiff film, typically a few 10–100 nm and GPa modulus, atop a thicker (mm) and softer (≈MPa), for instance an evaporated metal of a spun-coated glassy polymer supported by a polydimethylsiloxane (PDMS) elastomer. The mismatch in mechanical properties between films, provided that there is strong adhesion between them (to minimize delamination, crack formation, etc.), leads to surface buckling under strain. Strain can be induced thermally, by film evaporation/shrinkage, and commonly, by mechanical strain.

Plasma oxidation provides a facile route to generating a thin, glass-like film onto PDMS,[26] enabling precise control of film thickness growth kinetics.[27–29] We have previously demonstrated the design of tunable optical gratings[30] using this method (building on the previous demonstrations with polymer bilayer laminates[31]). The impact of the PDMS substrate thickness on the mechanochromic response of 1D plasma oxidized PDMS films has been recently reported,[32,33] and color tunability according to illumination and viewing angle examined. Recently, the incorporation of polystyrene nanoparticles and the use of wire-bar coating (yielding regular arrays) was demonstrated to produce both angle-independent and -dependent structural colors, upon plasma exposure and wrinkling.[34]

In this study, we build upon the structural color and mechanochromic response exhibited by 1D plasma oxidized wrinkled PDMS topographies ranging from nano to the micronscale, and quantitatively examines the emergence of color mixing, by superposition of diffraction orders of distinct colors at similar observation angles. We then quantify the joint roles of amplitude and periodicity in color brightness, and finally consider

A. Tan, L. Pellegrino, Z. Ahmad, J. T. Cabral
Department of Chemical Engineering
Imperial College London
London SW7 2AZ, UK
E-mail: j.cabral@imperial.ac.uk
A. Tan, J. T. Cabral
Centre for Processable Electronics
Imperial College London
London SW7 2AZ, UK
The ORCID identification number(s) for the author(s) of this article can be found under https://doi.org/10.1002/adom.202200964.

DOI: 10.1002/adom.202200964

color modulation and directionality with gradient wrinkles (i.e., surfaces with spatially varying periodicity) and multi-axial (bidirectional and isotropic) patterns that can be readily fabricated. We demonstrate both uniform and spatially varying colors with observation angle, and further expand the palette of pattern complexity by leveraging wrinkling wave superposition in both simultaneous and sequential steps,[35,36] to yield directional color resulting from the interference and relative orientation of wrinkling generations.

2. Results and Discussion

2.1. Plasma Oxidation of PDMS and Surface Wrinkling

Plasma oxidation of PDMS provides an effective means of generating glassy skin films onto bulk PDMS (and thus a bilayer) with precisely tunable thickness, which therefore yield a library of surfaces of varying wrinkling periodicity (d) and amplitude (A). By varying the strain field, a range of 1D, 2D, and isotropic structures can be formed. In short, if the plasma exposure is carried out under (pre-)strain conditions, wrinkled surfaces form upon strain relaxation, termed "on" samples; conversely, if plasma exposure is carried out when PDMS is in its relaxed state, then the sample is termed "off", and thus surface wrinkling is induced upon the (active) application of strain. Specifically, in this work we fabricate 1D structures by uniaxial mechanical strain, and isotropic structures by a thermal cycling treatment, expanding and contracting the bilayer as illustrated in **Figure 1**a. Furthermore, we take advantage of simultaneous and sequential wrinkling wave superposition to access different 2D topographies. By diffracting a narrow light beam (e.g., a laser), periodic 1D surfaces respond as planar (tunable) 1D phase gratings,[30,31] displaying a series of diffraction spots symmetric with respect to the direct beam (center), whose spacing in reciprocal space reflects the pattern periodicity in real space. Isotropic wrinkles yield single-frequency centro-symmetric diffraction patterns, with a circular annulus reflecting the average pattern periodicity, as shown in Figure 1b.

The mechanisms and kinetics of the frontal growth and propagation of the glassy skin layer on PDMS by oxygen plasma has been previously reported,[28,37] and can be effectively tuned by plasma power, oxygen pressure, and exposure time. Upon strain, the bilayer yields a sinusoidal profile with periodicity d and amplitude A which can be generally expressed as[38]

$$d = \frac{2\pi h(\overline{E}_f/(3\overline{E}_s))^{\frac{1}{3}}}{(1+\varepsilon)(1+\xi)^{\frac{1}{3}}} \tag{1}$$

$$A = \frac{h(\varepsilon/\varepsilon_c - 1)^{\frac{1}{2}}}{(1+\varepsilon)^{\frac{1}{2}}(1+\xi)^{\frac{1}{3}}} \tag{2}$$

where h is the glassy film thickness, $\overline{E}_f$ and $\overline{E}_s$ are, respectively, the in-plane strain moduli of the film and substrate, given by $\overline{E} = E/(1-\nu^2)$, where E is the Young's modulus and ν the Poisson ratio ($\simeq 0.5$ for PDMS); $\xi = 5\varepsilon(1+\varepsilon)/32$, accounting for the non-linearity of the stress– strain relationship of the substrate in the finite deformation regime (i.e., non-Hookean response). Note that we refer to d, instead of the customary surface wavelength λ, as the surface periodicity to avoid confusion with the wavelength of light. A critical strain must be exceeded to trigger the mechanical instability, ε_c

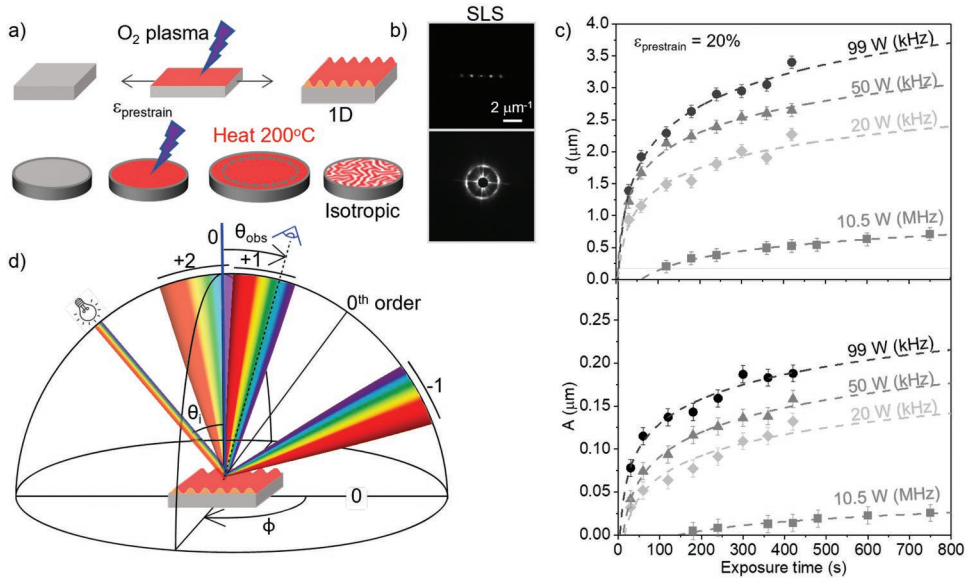

Figure 1. a) Schematic of the formation of 1D and isotropic wrinkling samples. 1D wrinkles: plasma oxidation on a prestrained PDMS elastomer coupon and relaxation of strain. Isotropic wrinkles: plasma oxidation on a flat, round PDMS elastomer coupon, heated to 200 °C for 30 min to induce strain through thermal expansion, and cooled to induce the wrinkles. b) Diffraction pattern for the 1D (99 W, 120 s) shows orders zeroth to second and a ring diffraction of first order for the isotropic (20 W, 120 s). c) Wrinkling periodicity (d) and amplitude (A) measured as a function of plasma exposure time (s) for treated PDMS coupons with different power and plasma frequency (13.6 MHz: 10.5 W; 40 kHz: 20, 50, and 99 W). d) Schematic of light diffraction of wrinkled samples showing up to three orders (–1, +1, +2): a white LED light at θ_i, observer/camera at θ_{obs}.

$$\varepsilon_c = \frac{1}{4}\left(\frac{3\overline{\overline{E}}_s}{\overline{\overline{E}}_f}\right)^{\frac{2}{3}} \quad (3)$$

In the low deformation limit ($\varepsilon \lesssim 0.1$), the amplitude alone depends on strain, thus allowing for d and A to be decoupled in surface patterning. At high strains ($\varepsilon \gtrsim 0.5$) sinusoidal patterns give rise to further modes, including the formation of folds, period-doubling, and ridges.[39] The experimentally measured logarithmic dependence of d and A on plasma exposure time,[28,37] for both a 13.6 MHz and 40 kHz plasma chambers employed in this work, is shown in Figure 1c. More complex wrinkling geometries, beyond 1D and isotropic gratings, were readily generated with different strain field or exposure arrangements. Gradient wrinkled surfaces, varying both periodicity and amplitude, can be fabricated using tapered PDMS coupons (which spatially vary ε),[40,41] or a stepped, or gradient, plasma oxidation process (with spatially varying h).[42–45] Multiaxial strain fields can induce a plethora of patterns; for instance 2D wrinkles can be fabricated, either through the simultaneous or sequential application of strain in two directions, yielding hexagonal, checkerboard, and herringbone wrinkled structures.[46–48] Sequential wrinkling approaches,[35,36] use surface wave superposition at varying angles (from 0° to 90°) to tune wrinkled surfaces from 1D to checkerboard, creating a variety of "s and ripple" structures, with additional in-plane (xy) periodicities. Representative topographies were designed and fabricated to yield desired optical effects detailed below.

2.2. Wrinkled Surfaces as Phase Gratings

Wrinkled bilayers have been used in the fabrication of diffraction gratings exhibiting mechanochromic properties,[49] whose diffraction pattern can be readily computed from Bragg's Law. For a incident light at an angle θ_i, the pathway difference between the incident light on the adjacent wrinkle crest is $d \times \sin\theta_i$, where d represents the wrinkling spacing. Similarly, the pathway difference between the reflected light on the adjacent wrinkle crest is $-d \times \sin\theta_r$, where θ_r is the angle of detection, yielding

$$n\lambda = d(\sin\theta_i + \sin\theta_r) \quad (4)$$

where integer n is the diffraction order of light wavelength λ. Tunable phase gratings have been previously demonstrated in case of thin polymer films deposition or lamination onto an elastomeric foundation,[31,50,51] giving access to a variable distribution of energy in the diffraction orders. In a phase grating, the resulting diffraction pattern can be modeled for all diffraction orders p according to[31,52]

$$I \approx \sum_{p=-\infty}^{\infty} J_p^2\left(\frac{m}{2}\right) sinc^2\left[\frac{W}{\pi}\left(q - \frac{2p\pi}{d}\right)\right] \quad (5)$$

where J_p is a Bessel function of the first kind, W is the half-width of the aperture, d is the wrinkling periodicity, $m/2$ is the maximum phase shift impart to the light, and p is an index accounting for the pth diffraction order. Often $W \simeq 0.5$ mm, determined by the typical profile of laser beam (in the Fraunhofer limit conditions). The maximum intensity of the pth order can be approximated to be proportional to the Bessel function $J_p^2(m/2)$ as the sinc function is narrowly distributed in q about each order without significant overlap between adjacent orders. The phase contrast, $m(\Delta)$ can be rationalized in terms of the wrinkling bilayer model of amplitude, $A(\varepsilon)$ by

$$\frac{m(\varepsilon)}{2} = 2\pi\frac{A(\varepsilon)}{\lambda}[n-1] \quad (6)$$

where $A(\varepsilon)$ is extracted from the wrinkling high deformation model (Equation (2)), n is the refractive index, and λ the light wavelength. In a simple bilayer with a sufficiently thin skin, the refractive index n can be approximated by that of the bulk material.[31]

In a 1D wrinkled sample, light diffraction is perpendicular to the direction of the wrinkles (Figure 1d). For sufficiently large wrinkling periodicity, multiple orders of diffracted light can be observed, where positive orders are denoted as those in between the incident light and the reflected 0th order, and conversely for negative orders. The observation angle θ_{obs} represents the position of the observer or camera. The variation in θ_{obs} allows for different structural colors to be viewed.

2.3. Structural Color from Nano- to Microscale Wrinkles

Diffraction of white light from wrinkled surfaces, acting as phase gratings, can yield brilliant structural colors which depend on pattern periodicity d as well as observation angle θ_{obs}. Such colors are optimally observed by minimizing light reflection and scattering from the substrate. This can be achieved through doping the PDMS elastomer, for instance with carbon-black, resulting in uniform light absorbance in the visible range (Figures S1 and S2, Supporting Information). Depending on the plasma oxidation conditions and strain, the wrinkling periodicity and amplitude can be precisely tuned to select the color observed from the surface. The relation between pattern topography and observation diffraction angle, given by Equation (4) enables the prediction of the color wavelength λ at all angles, $0° \geq \theta_{obs} \geq 90°$, for instance when the incident white light is normal to the sample surface ($\theta_i = 0°$). Practically, beyond $\theta_{obs} = 70°$, the observer's field of the surface becomes restricted. **Figure 2**a shows the first diffraction order for wrinkled surfaces with periodicities up to d = 800 nm. When wrinkles display periodicities shorter than the wavelength of visible light, no color will be seen to be diffracted from the surface. In these regions, UV and X-ray diffraction could be accessed. MHz plasma oxidation allows for the fabrication of sub-micron structures, yielding single structural color diffraction at accessible observation angles. By varying the plasma exposure time, d ranging from 490–710 nm were achieved as shown in atomic force microscopy (AFM) micrographs in Figure 2b. The resulting diffracted colors were captured at different θ_{obs}. For d = 490 nm, diffracted wavelengths are limited to larger θ_{obs}, where color is only accessible beyond 60° (Figure 2c(i)). As plasma exposure time increases, resulting in larger d, a red-shift is observed with θ_{obs} with colors detected

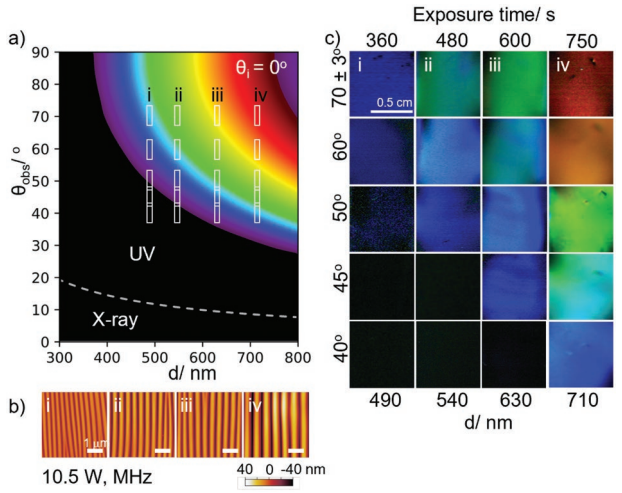

Figure 2. a) Nano-wrinkled samples formed using 10.5 W, MHz plasma displaying discrete angular dependency of colors when white light is shone normal to the sample, $\theta_i = 0°$. Color observed in the first order with observation angle θ_{obs} and wrinkling periodicity, d up to 800 nm. White boxes indicates the region of colors accessible (±3°) for each sample (i–iv), at different θ_{obs}, corresponding to Figure 2c. Below the threshold light wavelength of 380 nm, diffraction limits of UV and X-ray are reached. b) AFM scans corresponding to the samples (i–iv). c) Single color diffraction observed in plasma-treated samples at exposure times of 360, 480, 600, and 750 s yielding periodicities of 490, 540, 630, and 710 nm respectively.

at lower observation angles. When $d = 710$ nm, a red color can be observed for $\theta_{obs} = 70°$ (Figure 2c(iv)).

In the case of micron-scale surface wrinkles, additional diffraction orders can be observed. The diffraction orders, initially discrete and well separated at low surface periodicities, start to overlap resulting in color mixing when $d \gtrsim 1.1$ µm. The color mixing arises from the contribution of different diffraction orders at the same θ_{obs} at fixed periodicity. **Figure 3**a shows the expected resulting colors by taking into consideration diffraction order mixing (computed by expressing and combined each diffracted color in RGB format). Plasma oxidation at KHz, performed at 99 W at different exposure times, allows the development of d ranging from 1.3–3.4 µm (Figure 3b). The observed colors at varying θ_{obs} are shown in Figure 3c, with the contributing orders labeled within each image. When $d = 1.3$ µm, single color diffraction is observed until $\theta_{obs} \geq 60°$ where the resulting "magenta" color is a contribution from the second and third order. As the wrinkle wavelengths increase, the overlap of two or more orders results in non-discrete colors. Illumination with a red light instead ($\lambda \approx 650$ nm), induces diffracted red colors at different intensities as the contribution in red increases with the wrinkling periodicity d (Figure S3, Supporting Information).

Theoretically, diffraction intensities for colored wrinkled structures can be quantified for each order modifying Equation (5) to account for the gradient glassy skin[30]

$$I(\overline{x},\gamma) \approx \sum_{i=0}^{8} A_0 e^{-kn_i} I_{ni}(x,\gamma) \tag{7}$$

where n_i ranges from 1.41–1.55, $A_0 = 8.0 \times 10^{18}$, and $k = 31.5$. From this, we use the relationship between exposure time with d and A to compute an intensity plot, which is also dependent on the wavelength of light λ. We would expect that for a given condition and diffraction order, the intensity of a longer wavelength of light like red light (760 nm) would have a lower intensity than a violet light (380 nm). In Figure S4a, Supporting Information, the theoretical dependence of diffraction intensities with exposure time for different wavelengths of light—from violet of 380 nm to red of 760 nm are plotted for the first

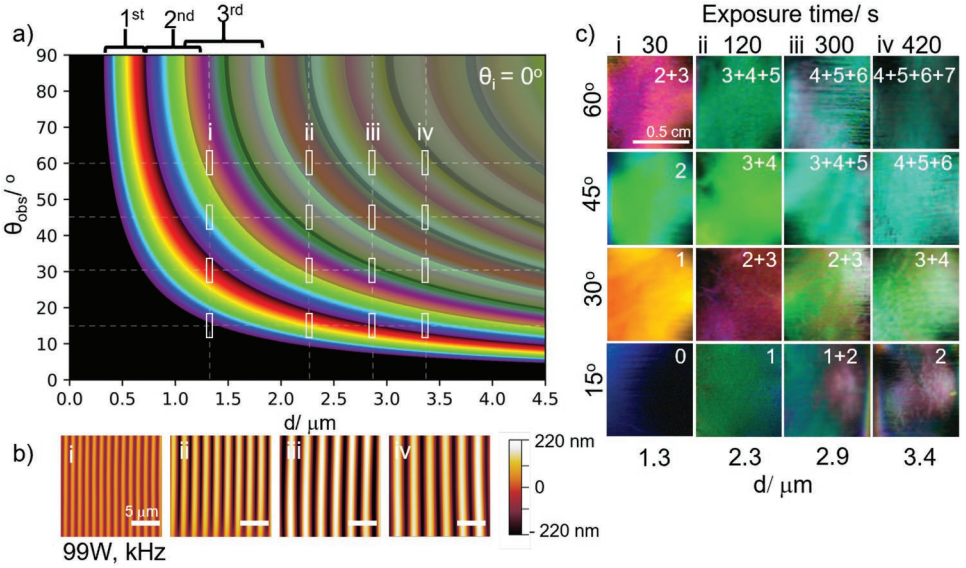

Figure 3. a) Micro-wrinkled samples formed using 99 W, kHz plasma exhibiting colors contributed from up to seven diffraction orders. From the second diffraction order, overlap of different orders becomes prominent, resulting in mixed colors with increasing angles. b) AFM scans corresponding to the samples (i–iv). c) Color diffraction for plasma-treated samples at $p = 99$ W and exposure time of 30, 120, 300, and 420 s yielding wavelengths of 1.3, 2.3, 2.9, and 3.4 µm, respectively. The diffraction orders contributing to the final color are reported at the top right corners of each condition.

order. The intensity for larger wavelength of light are lower and the intensities can be seen to modulate with exposure time, as a result of the evolution of wrinkling periodicity and amplitudes. With increasing order, it is expected that the intensities of light decrease for a single wavelength. In Figure S4b, Supporting Information, the plot of intensities for 533 nm wavelength of light is shown from the first tosixth order. Due to the spread of intensities from shorter to longer wavelength, intensity of different colors from adjacent orders can occur. Indeed, the intensities for longer wavelengths of the fifth order would overlap with those of the shorter wavelengths from the sixth.

2.4. Mechanochromic Response: Tuning Colors with Strain

The mechanochromic response of wrinkled surfaces can be tuned modulating the compressive strain release after the plasma oxidation step. The sensitivity in color variation can be adjusted by considering the relationship between pattern periodicity d and strain, ensuring that only the first diffraction order ($n = 1$) contributes at the accessible θ_{obs}, to avoid color mixing. The bilayer film parameters can be designed to achieve the appropriate periodicity range. For a system with a smaller periodicity change under strain, (single) color sensing would be optimal with surfaces of smaller wrinkling periodicity at higher θ_{obs}; conversely with larger periodicity changes, sensing would be optimal with surfaces of larger d at lower θ_{obs}, as detailed in Figure S5, Supporting Information. The observed color at a given θ_{obs} can be readily calculated as a function of strain ε, by combining Equations (1)–(4) to yield

$$\lambda = \frac{2\pi h(\overline{E}_f/(3\overline{E}_s))^{\frac{1}{3}}}{(1+\varepsilon)(1+\xi)^{\frac{1}{3}}}\sin\theta_{obs} \tag{8}$$

Specifically, **Figure 4**a reports the color shifting from red (buckling onset) to blue (full release) as a function of compressive strain ε for a sample treated at $p = 50$ W and $t = \sim 30$ s and prestrained to 0.5. At a fixed θ_{obs}, the diffracted color observed can be manipulated by a change in the wrinkling periodicity, d. When $\theta_{obs} = 31°$, the spectrum of the rainbow can be observed when d is tuned between 0.9 and 1.5 µm as described in Figure 4b. Due to the intrinsic nature of the buckling relaxation process and as described by Equation (1), we are able to exploit this relationship to create tunable colors with strain. Indeed, the decrease of the wrinkling periodicity with strain fulfills the required range to tune the sample to the color of the spectrum. As the sample experiences compressive strain, the wrinkling amplitude increases with strain, therefore it is possible to determine the theoretical relationship with diffraction intensity through the previously established diffraction model in Equation (7). Following the ability to tune the wrinkling

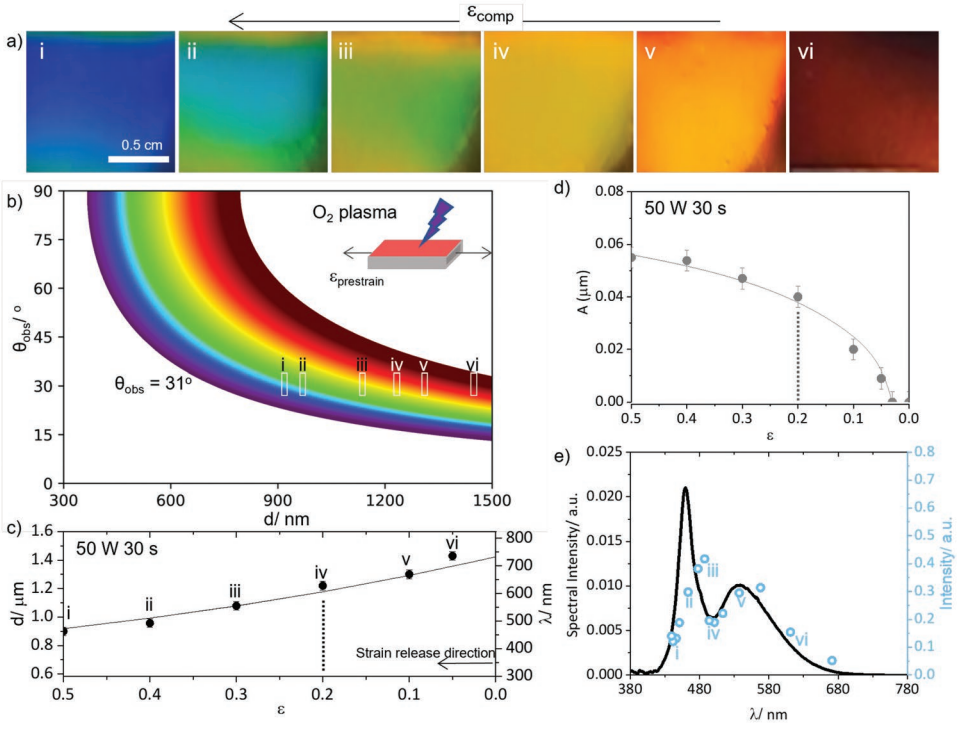

Figure 4. a) Mechanochromic variation in CB-PDMS samples oxidized at 50 W, 30 s undergoing compressive strains from (i) $\varepsilon = 0.5$ to (vi) $\varepsilon = 0.05$, at $\theta_{obs} = 31°$. b) First order colors observed at wrinkling periodicity from 300–1500 nm. Series of colors in the first order observed from $\lambda \approx 700$ nm (red), when $d \approx 1.4$ µm, to $\lambda \approx 450$ nm (blue), when $d \approx 900$ nm. White boxes (i–vi) correspond to the color areal region reported in (a). c) Wrinkling periodicity, d, as a function of strain for samples (i–vi). The solid line corresponds to Equation (1). Each d corresponds to an observed diffracted wavelength, λ on the right y-axis. d) Amplitude of wrinkles as a function of strain with the solid line corresponding to Equation (2). e) Calculated diffracted intensity (black line) as function of λ, parametrized by the white light and CB-PDMS absorbance across the spectrum. Measured intensities (blue points) were extracted via RGB decomposition (RGB/3) of (i–vi).

periodicity and amplitude with strain, we would expect the sample to experience a continuous increase in intensity from red to blue (Figure S4, Supporting Information). However, this model alone assumes an equal intensity of the white light at all wavelengths, and it is thus insufficient to explain the intensity exhibited by the samples at their respective colors. Unsurprisingly, there is an effect on the intensity of the light source with the resultant intensity of the color observed. Therefore, modeled color intensity was parametrized by the light spectrum and the absorbance of the CB-PDMS in the required range (Figure S6, Supporting Information). The light spectrum and absorbance were normalized, and combined with the previous description to attain the final model. The intensity of the samples were taken by normalizing the RGB values to one through ImageJ. From Figure 4e, we find that the experimental results agree well with the model, taking into account the spectrum of the light source.

2.5. Effect of Relative Illumination and Viewing Angles on Color Perception

The variation in incident angle of light with respect to the sample extends the range of colors observed for structures with smaller wrinkling periodicities instead of incident light normal to the sample. When the angle between the incident light and the camera is fixed at 50° with the sample being rotated along its axis, this allows for the simultaneous change in θ_i and θ_{obs} as reported in the schematic in **Figure 5**a(i–iii). By using Equation (4), we can predict the color wavelength while rotating the sample. Conventionally, when θ_{obs} and θ_i are on opposite sides with respect to the normal, θ_{obs} would be denoted as a negative angle. When a plasma treated sample with wrinkling periodicity of 490 nm is observed at θ_{obs} with a simultaneous change in θ_i, color wavelengths up to ≈650 nm in the first order can be viewed between 50° ≤ 70°, while no color can be seen at other angles (Figure 5a). By changing the incident light angle, the sample can exhibit up to a yellow hue when $\theta_i = 70°$ (Figure 5b), compared to the limited accessibility in color when θ_i is fixed at the normal, where only blue can be accessed at higher viewing angles (Figure 2c(i)). For d of 630 nm, three distinct orders (–1, +1, +2) can be observed while rotating the sample such that $0° \leq \theta_i \leq 70°$. Between $8° < \theta_i \leq 44°$, no color can be observed. At $0° \leq \theta_i \leq 8°$, the –1 order can be seen, the +1 order at $44° \leq \theta_i \leq 70°$, and +2 order at $68° \leq \theta_i \leq 70°$ (Figure 5c). As a result, up to a red hue at $\lambda = 760$ nm is observable when $\theta_i = 70°$ and $\theta_{obs} = 20°$, as compared to a green visible when θ_i is fixed at 0° (Figure 2c(iii)).

2.6. Azimuthal Viewing Angle and Color of 1D and Isotropic Wrinkles

1D surfaces have structural colors limited to the direction of diffraction. When a 1D sample (kHz, 99 W, 60 s) is rotated about ϕ ($\theta_i = 0°$, $\theta_{obs} = 40°$), the intensity of the colored sample can be monitored and observed as function of the angle as showed in **Figure 6**a. When $\phi = 0$, the intensity of the sample, measured by (R + G + B)/3 can be seen at a maximum. As ϕ increases, the

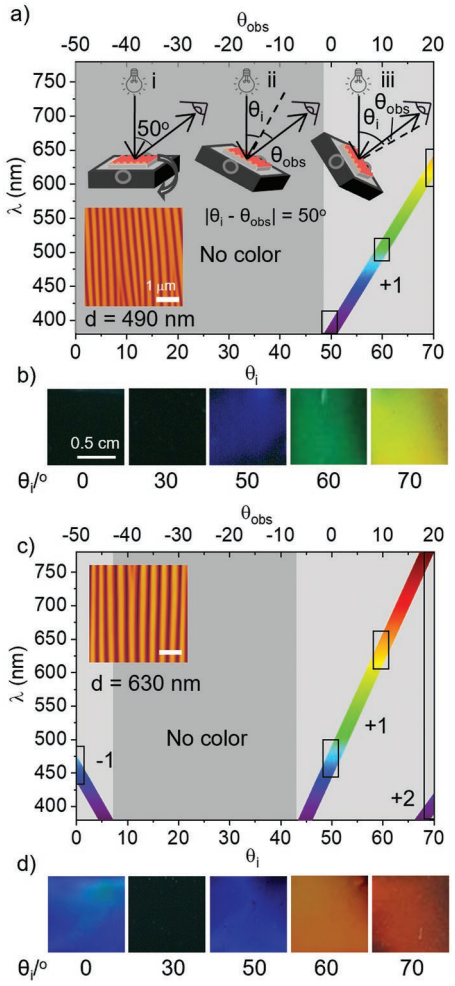

Figure 5. a) Color variation observed changing simultaneously θ_i and θ_{obs}, for a MHz plasma-treated sample at 10.5 W, 360 s yielding d of 490 nm. b) Images of sample showing increase range of accessible wavelength diffracted compared to in Figure 2c(i) with blue color observed at 50° while yellow at 70°. c) Color variation observed on a sample for MHz plasma-treated sample at 10.5 W, 600 s yielding d of 630 nm. Light can be observed to be diffracted in –1 order from 0° to 6°, +1 order from 45° to 68°, and +2 order from 68° to 70°. d) Images of sample showing corresponding diffracted colors.

intensity can be seen to decrease until it reaches a minimum at $\phi \approx \pi/6$ (Figure 6b). This occurs when the direction of diffraction of the sample becomes out of line with the observer. As the diffraction of sinusoidal wrinkles are perpendicular to the wrinkle direction, this only allows observance of the color in one axis with respect to the sample (Figure 6c). The inset shows the first diffraction order pattern of a 1D structure.

In order to increase the viewing angle of structural colors, isotropic wrinkles can be employed. When an isotropic sample is fabricated under the same plasma conditions, it exhibits structural color as the sample rotates 2π about ϕ. The intensity (a.u.) of the color was measured to be comparatively lower between 40°–60° while undergoing rotation, displaying color at every ϕ ($\theta_i = 0°$, $\theta_{obs} = 40°$) as reported in Figure 6d. These isotropic structures have a ring diffraction pattern, diffracting light in all directions. Due to the light being diffracted in all

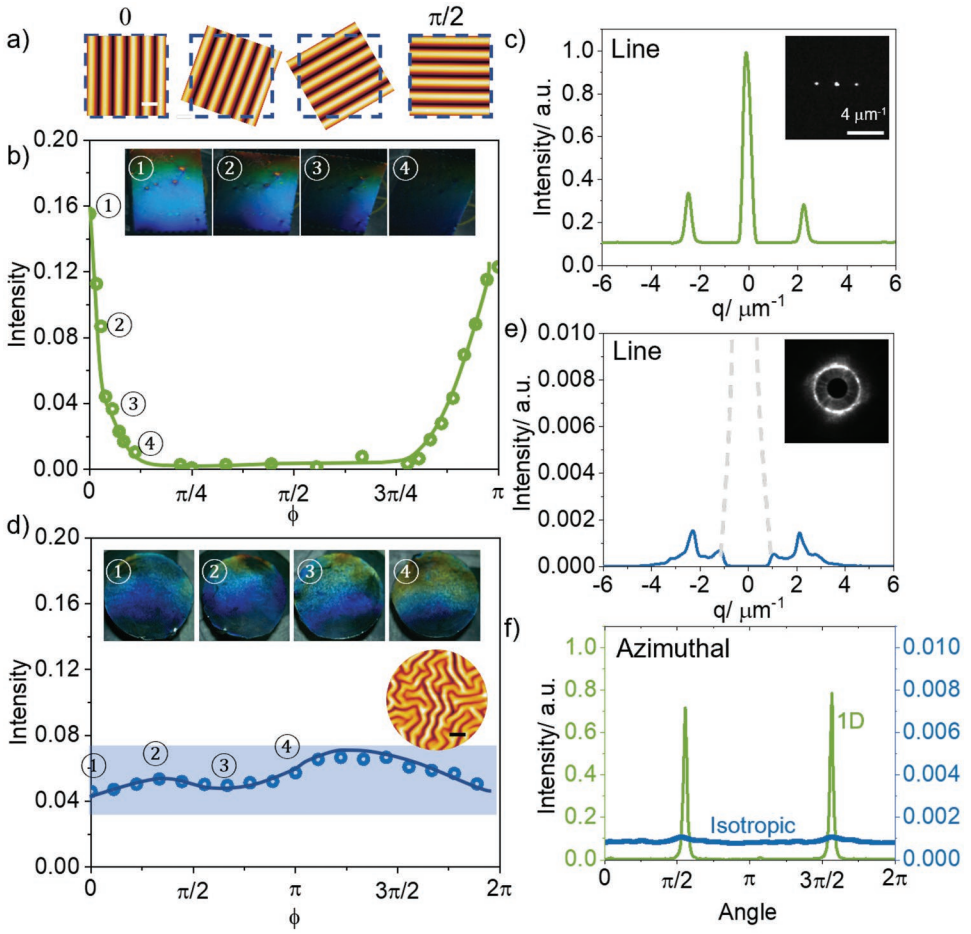

Figure 6. a) Schematic of the rotation of wrinkled sample along ϕ. b) Plot of normalized intensity for a 1D sample (kHz plasma, 99 W, 60 s) with ϕ shows a decreasing intensity from 0 to $\pi/6$. c) The 1D diffraction pattern intensity where zeroth and first diffraction orders are shown, with the light scattering image shown in the inset. d) Plot of normalized intensity for an isotropic sample (kHz plasma, 99 W, 60 s) when rotated along ϕ. e) The diffraction intensity of isotropic diffraction along a line. The gray dotted line reflects the middle beam where a beam stopped was used. f) Azimuthal averages for 1D and isotropic diffraction patterns. In the 1D diffraction, two intensity peaks are seen which reflects the positions of observed structural color. In the isotropic, the azimuthal average stays relatively in a constant range of 0.001, reflecting structural color 2π about ϕ.

directions, the line diffraction pattern is of a much lower intensity than the peaks in the 1D. An azimuthal average measurement can be used to clearly show the comparison between the two structures. In the 1D diffraction, two distinct intensity peaks are seen, reflecting the position of structural color observation. In the isotropic sample, the azimuthal average stays relatively constant, with structural color reflected about 2π of ϕ.

2.7. Homogeneity and Directional Color

An implication arising from the fabrication of regular 1D wrinkling structures with homogenous wrinkling periodicity is a characteristic "rainbow" color perceived especially for large areas, which is enhanced at a close observation distance. As the colors viewed are sensitive to θ_{obs}, a small change can lead to different colors being seen at a single wrinkle periodicity. The spread of color occurs as the light reaching the observer has different viewing angles from the top and bottom of the sample (θ_{obs1} and θ_{obs2}, respectively), thus yielding different wavelengths (λ_1. λ_2) (**Figure 7**a). The respective θ_{obs} can be calculated with respect to the position of the observer

$$\theta_{obs1} = 90 - arctan\frac{L}{h} \tag{9}$$

$$\theta_{obs2} = 90 - arctan\frac{(L-W)}{h} \tag{10}$$

where h and L describes the vertical and horizontal position of the observer, and W the distance between the observed reflected light. Conversely, it is possible to create a variable structure to create local spatial periods required to only see a specific color, depending on the position of the observer (Figure S7, Supporting Information). Previously, Voisiat et al., have demonstrated that the homogeneity of large samples can be improved through creating varying periodic spacing using direct laser interference patterning.[53] Gradient wrinkling topographies can be induced either tuning the thickness of the exposed glassy skin generated by plasma oxidation or by applying a gradient strain field, changing the geometry of the sample and therefore

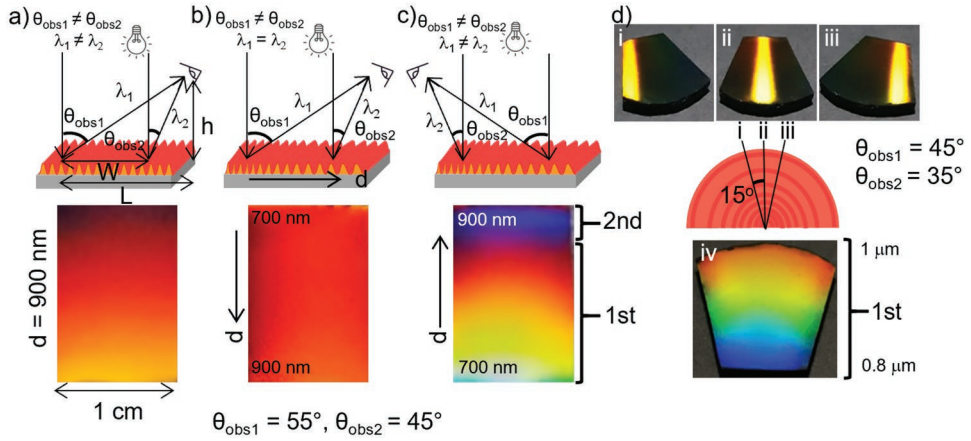

Figure 7. Structural color behavior at various observation angles for a) a 1D wrinkle surface, displaying a heterogenous colored surface; b) step-wise gradient 1D wrinkles, observed from the longest periodicity (d = 900 nm), showing a homogeneous red color. c) The same sample in (b), observed from the shortest periodicity (d = 700 nm), exhibiting an accentuated "rainbow" effect. d) Samples prepared employing geometric graded coupons, exhibiting curved wrinkles directional color when rotated about ϕ, (i–iii) show homogeneous strips of yellow while (iv) showing a "rainbow" effect.

altering the strain components. The resulting periodicity gradient can produce a distinct diffracted wavelength of light at a given angular range. In both methods, no significant variation of the wrinkling amplitude was observed, thus with a negligible impact on the color intensity. For the first approach, here referred to as step-wise plasma oxidation, different sections of the same area treated at different exposure times, yielding varying periodicities and amplitudes. As the exposure time for an area increases, this give rise to larger periodicity and amplitudes. When a stepwise sample (Figure S8, Supporting Information) is viewed from a position with L = 10 cm, W = 3 cm, and h = 7 cm, this gives rise to θ_{obs1} = 55° and θ_{obs2} = 45°. The resulting wrinkling periodicities, ranging 700–900 nm, when viewed from the end of the sample with largest periodicity, exhibit a homogeneous red color spanning the entirety of the sample, as $\lambda_1 = \lambda_2$. Conversely, when the same gradient structured sample is viewed from the other end of the sample, the "rainbow" effect of colors are accentuated, where the periodic change leads to an even greater variation in color observed (Figure 7b,c).

The second approach allows for the fabrication of varying periodic structure by altering the geometry of the stretched sample, by using a trapezoidal shape for example (Figure S9, Supporting Information). When a non-rectangular shape undergoes an extensional or compressive uni-axial strain, the magnitude of the strain will scale with the sample surface area. In the case of a trapezoidal shape, this induces a torsional strain field that is reflected in a curvature of the wrinkling pattern. The sample experiences a higher strain at the narrow side, and lower strain on the wider side. The overall patterns can be rationalized as a damped sine wave evolving from the narrow side, or higher strain region. The curve graded wrinkles display directional structural color, as the 1D wrinkles can only diffract perpendicular to the wrinkling direction (Figure 7d). When the wrinkles are convex with respect to the viewer, the sides of the sample are such that it diffracts color out of plane with respect to the center of the sample. Strips of homogeneous color can be manipulated and seen dependent on the viewing angle ϕ. When ϕ = 0°, a strip in the center can be seen (Figure 7d(i)). Upon rotation of ±15°, the strip of color can be seen to move toward the edge of the sample (Figure 7d(ii, iii)). When the sample is positioned such that the wrinkles concave with respect to the viewer, the diffraction of the wrinkles converge onto the viewer and a "rainbow" effect can be seen to be exhibited by the entire sample (Figure 7d(iv)). Similarly, we have also demonstrated that these varying periodic structures can be extended beyond the 1D to isotropic samples. Such radial-gradient isotropic samples exhibit "rainbow" colors in a crescent formation, attributed to the change in periodicity across the sample as well as θ_{obs}, as detailed in Figure S10, Supporting Information.

The idea of directionality of wrinkle surfaces can be extended to that of 2D structures, where we can further manipulate the colors exhibited depending on the observer's perspective. As previously mentioned, 2D structures can be fabricated through either a simultaneous or sequential step,[35,36,46] where the sequential step can be performed at different angles. A symmetrical checkerboard was achieved through a sequential step performed at 90° with the conditions stated in the Experimental Section, achieving d = 680 nm. When observed at θ_{obs} = 40°, a blue structural color can be observed at intervals of 90° along ϕ, with no color exhibited at other angles, reflecting the orthogonal superimposed first and second generation wrinkling waves, respectively at ϕ = 0° and ϕ = 90°. Therefore, the overall structural color is exhibited only alongside the specific generation orientation and not visible at other angles. On the other hand in a herringbone structure, arising from the simultaneous relaxation of a two-directional strain field, structural color can be observed for different ϕ, however with varying intensities. Specifically, at ϕ = 0°, a lower intensity is observed progressively increasing at ϕ = 45° and ϕ = 90°. This can be ascribed to the more complex intrinsic morphology exhibited by the herringbone pattern, where the color observed at ϕ = 45° is given by the overlap of two different periodicity, namely a "long" d (xy plane) along ϕ = 90°, giving a stronger blue reflectance, a "short" d (xz plane) showing a dimmer blue color. For "sand ripple" patterns, generated by sequential wrinkling superposition, and in this case a 20° pattern (**Figure 8**c), is able to exhibit color up to ϕ rotation of 45°. Initially when ϕ is at 0°, the contribution of

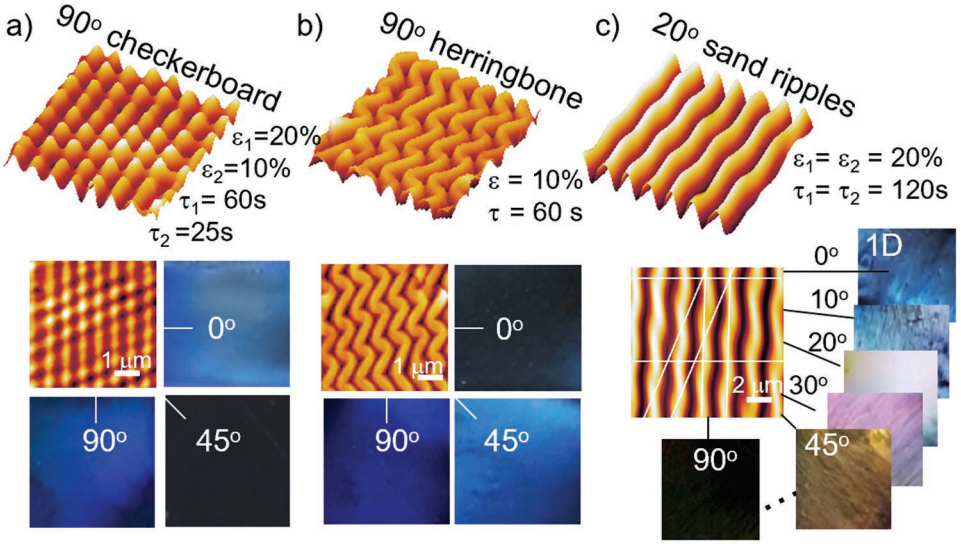

Figure 8. Structural color in 2D wrinkled surfaces. a) Symmetrical checkerboard exhibiting colors in phases of 90°. At θ_{obs} of 40°, a blue can be seen at $\phi = 0°$ and $\phi = 90°$ which "switches off" at $\phi = 45°$. b) In a herringbone structure, a rotation through $\phi = 0°$– 90° shows a blue hue that varies in intensity. c) A 2D 20° "sand ripple" structure exhibiting a blue color as a result of the second generation 1D structure at $\phi = 0°$. As ϕ increases, it transitions to a yellow hue until beyond 45° where it goes beyond the direction of diffracted light.

color is primarily due to the second generation of wrinkles. As ϕ increases, color mixing arises reaching $\phi = 20°$, orientation of the first generation pattern, transitioning from a blue to a yellow and opalescent shade. From $\phi = 45°$, the overall structural color decreases in intensity and ultimately at $\phi = 90°$ the only contribution to the overall structural color is given by λ_{xy}, arising from the superposition of the two wrinkling waves.

3. Conclusions

In this paper, we demonstrate the generation of both simple and intricate tunable structural color response in 1D and 2D (biaxial and sequential) and isotropic wrinkling patterns, fabricated by plasma oxidation of PDMS and mechanical or thermally-induced buckling. From the inspection of the mechanochromic response in both micron and nanoscale 1D wrinkling structures we benchmark and quantify the impact of surface periodicity in the accessible colors. From these consolidated foundations, we evaluate the effect of color mixing induced by overlap of multiple diffraction orders. We establish quantitative relations between color intensity, the interplay between illumination and viewing angles, accounting for the wrinkling mechanics and diffraction phenomena. Our model incorporates the gradient nature of the glassy skin, alongside the established phase grating optics system, to quantitatively model the intensity of the various diffraction orders. We inspect the effect of complex topographies on the structural color response, inducing a gradient in pattern periodicity and amplitude by either tuning the glassy skin thickness (via stepwise exposure) or by inducing gradient strain field (via a non-rectangular sample geometry, e.g., trapezoidal). We demonstrate how these surface patterns exhibit either spatially uniform color or enhanced "rainbow" color depending on the observation angle. Furthermore, we report isotropic wrinkled surfaces exhibiting color at all ϕ angles, that is, " around" the patterned surface. We explore the concept of optical and color directionality by creating multi-frequency patterns, achieved by superposing two independent wrinkling waves onto the *same* surface (by analogy to birefringent media), fabricated either by the application of a simultaneous bi-axial strain (in which the two wrinkling generations are strongly coupled) or a sequential wrinkling process with greater flexibility in d and A of each generation, as well as their relative angle, and thus of the corresponding optical axes. Overall, we expect our findings to be relevant to a range of applications such as packaging, smart displays, wearable electronic devices, and sensors.

4. Experimental Section

A carbon-black PDMS (CB-PDMS) (Sylgard 184, Dow Corning) substrate was prepared by casting a mixture of prepolymer, curing, and carbon black acetylene powder (50% compressed, 99.9+%, VWR) at a 10:1:0.03 mass ratio for 1D and 2D samples, and a mass ratio of 20:1:0.03 for isotropic samples. The mixture was stirred vigorously, degassed under vacuum, deposited onto a glass plate and cured at 75 °C in a convection oven for 1 h to crosslink into an elastomer with the resultant CB-PDMS with a thickness of 2.5 mm.

Surface plasma oxidation of the samples were performed using two different plasma chambers: a 13.6 MHz Harrick Plasma PDC-002 at P = 10.5 W for sub-micron wrinkle periodicity samples, and a 40 kHz Diener plasma (Femto), fitted with a pressure sensor (TM 101, Thermovac) at P = 20, 50, and 99 W and variable exposure times for samples with a larger wrinkle periodicity. Oxygen (BOC, 99.5%) supplied both plasma chambers. The chambers were evacuated to a pressure of 0.2 mbar, before flowing the gas for 5 min until the desired pressure was reached and stabilized. The plasma was then ignited, at the required power and exposure time.

1D, regular periodic sinusoidal patterns were fabricated through uniaxial strain of a PDMS coupon (2.5 cm × 2.5 cm) using a strain stage. The applied prestrain was calculated with respect to the initial (L_0) and final distance (L_1) between the clamps, $\varepsilon_{prestrain} = \frac{L_1 - L_0}{L_0}$.

The sample was stretched with a prestrain of 0.2, before it undergo plasma oxidation and subsequently released to form sinusoidal wrinkles. Samples with a varying periodic structure were fabricated either by a step-wise plasma oxidation or by changing the geometry of the sample to a trapezoidal shape.

2D samples were fabricated through either a simultaneous or sequential step. The simultaneous 90° sample was created through a biaxial strain of 10% of a PDMS coupon which undergo plasma treatment (P = 20 W, ε = 0.1) before the simultaneous release of strain to form a herringbone structure. 2D wrinkles through a sequential step were created through the replication of a 1D sample on fresh PDMS, followed by a second generation strain and plasma at an angle before the release. For a 90° symmetrical checkerboard, the first generation was performed at P = 20 W, τ = 60 s, ε = 0.2, and the second generation at P = 20 W, τ = 25 s, ε = 0.1. The 20° sand ripples were fabricated with the same conditions in both the generations, P = 20 W, τ = 120 s, ε = 0.2. Isotropic samples were fabricated through the plasma treatment of an unstretched circular CB-PDMS coupon (2.5 cm radius) which then undergo thermal heating to 200 °C for 30 min and cooled to room temperature to form the isotropic wrinkles.

Surface topographies were characterized by AFM using a Bruker Innova microscope, in tapping mode at 0.2 Hz, equipped with Al-coated Si tips (MPP-11100-W, Bruker) and analyzed with the in-built Nanoscope software. The mechanochromic phenomena were observed and recorded on a Basler acA2040-90uc camera with a white light source (Advanced Illumination) in a dark environment, which were then analyzed with ImageJ software.

Supporting Information

Supporting Information is available from the Wiley Online Library or from the author.

Acknowledgements

The authors thank Procter & Gamble and the EPSRC-funded Plastic Electronics CDT for a Ph.D. scholarship (Grant No. EP/L016702/1) and the Royal Academy of Engineering (RAEng, UK) for funding and a research chair.

Conflict of Interest

The authors declare no conflict of interest.

Data Availability Statement

The data that support the findings of this study are available from the corresponding author upon reasonable request.

Keywords

mechanochromic, polydimethylsiloxane, plasma-oxidation, structural color, tunable, wrinkling superposition, diffraction grating

Received: April 25, 2022
Published online:

[1] M. Srinivasarao, *Chem. Rev.* **1999**, *99*, 1935.
[2] P. Vukusic, J. R. Sambles, *Nature* **2003**, *424*, 852.
[3] S. Kinoshita, S. Yoshioka, J. Miyazaki, *Rep. Prog. Phys.* **2008**, *71*, 076401.
[4] B.-K. Hsiung, R. H. Siddique, D. G. Stavenga, J. C. Otto, M. C. Allen, Y. Liu, Y.-F. Lu, D. D. Deheyn, M. D. Shawkey, T. A. Blackledge, *Nat. Commun.* **2017**, *8*, 2278.
[5] P. Vukusic, J. Sambles, C. Lawrence, R. Wootton, *Proc. R. Soc. London, Ser. B* **1999**, *266*, 1403.
[6] D. Gur, B. A. Palmer, S. Weiner, L. Addadi, *Adv. Funct. Mater.* **2017**, *27*, 1603514.
[7] J. Teyssier, S. V. Saenko, D. Van Der Marel, M. C. Milinkovitch, *Nat. Commun.* **2015**, *6*, 6368.
[8] A. Saito, K. Yamashita, T. Hattori, Y. Kuwahara, *Jpn J. Appl. Phys.* **2022**, *61*, SD0801
[9] Z. Dong, H. Zhao, L. Nie, S. Tang, C. Li, X. Wang, *Front. Phys.* **2022**, *792*, 806904.
[10] H. Wang, K.-Q. Zhang, *Sensors* **2013**, *13*, 4192.
[11] H. S. Lee, T. S. Shim, H. Hwang, S.-M. Yang, S.-H. Kim, *Chem. Mater.* **2013**, *25*, 2684.
[12] W. Yang, S. Xiao, Q. Song, Y. Liu, Y. Wu, S. Wang, J. Yu, J. Han, D.-P. Tsai, *Nat. Commun.* **2020**, *11*, 1864.
[13] F. Cheng, J. Gao, T. S. Luk, X. Yang, *Sci. Rep.* **2015**, *5*, 11045.
[14] K. Yamashita, K. Kunitsu, T. Hattori, Y. Kuwahara, A. Saito, *Opt. Express* **2021**, *29*, 30927.
[15] Z. Xuan, J. Li, Q. Liu, F. Yi, S. Wang, W. Lu, *Innovation* **2021**, *2*, 100081.
[16] G. Chen, W. Hong, *Adv. Opt. Mater.* **2020**, *8*, 2000984.
[17] Q. Zhou, J. G. Park, J. Bae, D. Ha, J. Park, K. Song, T. Kim, *Adv. Mater.* **2020**, *32*, 2001467.
[18] X. Huang, Y. Hai, W.-H. Xie, *Theor.Appl. Mech. Lett.* **2017**, *7*, 169.
[19] C. Chen, C. A. Airoldi, C. A. Lugo, R. K. Bay, B. J. Glover, A. J. Crosby, *Adv. Funct. Mater.* **2021**, *31*, 2006256.
[20] M. Nixon, A. Orr, P. Vukusic, *J. R. Soc., Interface* **2015**, *12*, 20140749.
[21] J. H. Oh, J. Y. Woo, S. Jo, C.-S. Han, *ACS Appl. Mater. Interfaces* **2019**, *11*, 26442.
[22] C. A. Airoldi, C. A. Lugo, R. Wightman, B. J. Glover, S. Robinson, *Cell Rep.* **2021**, *36*, 109715.
[23] L. Zhou, L. Yang, Y. Liu, Z. Xu, J. Yin, D. Ge, X. Jiang, *Adv. Opt. Mater.* **2020**, *8*, 2000234.
[24] Z. Mao, S. Zeng, K. Shen, A. P. Chooi, A. T. Smith, M. D. Jones, Y. Zhou, X. Liu, L. Sun, *Adv. Opt. Mater.* **2020**, *8*, 2001472.
[25] J. Li, X. Lu, Y. Zhang, X. Ke, X. Wen, F. Cheng, C. Wei, Y. Li, K. Yao, S. Yang, *Adv. Funct. Mater.* **2021**, *31*, 2102350.
[26] N. Bowden, W. T. Huck, K. E. Paul, G. M. Whitesides, *Appl. Phys. Lett.* **1999**, *75*, 2557.
[27] A. Chiche, C. M. Stafford, J. T. Cabral, *Soft Matter* **2008**, *4*, 2360.
[28] F. A. Bayley, J. L. Liao, P. N. Stavrinou, A. Chiche, J. T. Cabral, *Soft Matter* **2014**, *10*, 1155.
[29] G. Ferretti, M. Nania, O. Matar, J. T. Cabral, *Langmuir* **2016**, *32*, 2199.
[30] A. Tan, L. Pellegrino, J. T. Cabral, *ACS Appl. Polym. Mater.* **2021**, *3*, 5162.
[31] C. Harrison, C. Stafford, W. Zhang, A. Karim, *Appl. Phys. Lett.* **2004**, *85*, 4016.
[32] Z. Li, Y. Liu, M. Marin, Y. Yin, *Nano Res.* **2020**, *13*, 1882.
[33] K. Wu, T. Zhu, L. Zhu, Y. Sun, K. Chen, J. Chen, H. Yuan, Y. Wang, J. Zhang, G. Liu, X. Chen, J. Sun, *Nano Lett.* **2022**, *22*, 2261.
[34] Y. Qi, C. Zhou, S. Zhang, Z. Zhang, W. Niu, S. Wu, W. Ma, B. Tang, *Dyes Pigm.* **2021**, *189*, 109264.
[35] L. Pellegrino, S. Khodaparast, J. T. Cabral, *Soft Matter* **2020**, *16*, 595.
[36] L. Pellegrino, A. Tan, J. T. Cabral, *Phys. Rev. Lett.* **2022**, *128*, 058001.
[37] M. Nania, O. K. Matar, J. T. Cabral, *Soft Matter* **2015**, *11*, 3067.
[38] H. Jiang, D.-Y. Khang, J. Song, Y. Sun, Y. Huang, J. A. Rogers, *Proc. Natl. Acad. Sci. USA* **2007**, *104*, 15607.
[39] Q. Wang, X. Zhao, *Sci. Rep.* **2015**, *5*, 8887.
[40] S. Raayai-Ardakani, J. Luis Yagüe, K. K. Gleason, M. C. Boyce, *J. Appl. Mech.* **2016**, *83*, 121011.
[41] C. Gao, Y. Li, *Int. J. Solids Struct.* **2017**, *104*, 92.

[42] J. S. Lee, H. Hong, S. J. Park, S. J. Lee, D. S. Kim, *Microelectron. Eng.* **2017**, *176*, 101.
[43] B. A. Glatz, A. Fery, *Soft Matter* **2019**, *15*, 65.
[44] L. Ma, L. He, Y. Ni, *J. Appl. Phys.* **2020**, *127*, 111101.
[45] S. Hiltl, J. Oltmanns, A. Böker, *Nanoscale* **2012**, *4*, 7338.
[46] X. Chen, J. W. Hutchinson, *J. Appl. Mech.* **2004**, *71*, 597.
[47] X. Chen, J. W. Hutchinson, *Scr. Mater.* **2004**, *50*, 797.
[48] C. S. Davis, A. J. Crosby, *J. Polym. Sci., Part B: Polym. Phys.* **2012**, *50*, 1225.
[49] S. Chen, T. Ma, J. Bai, X. Ma, J. Yin, X. Jiang, *Adv. Sci.* **2020**, *7*, 2002372.
[50] Y. Meng, X. Gong, Y. Huang, L. Li, *Appl. Mater. Today* **2019**, *16*, 474.
[51] C. Yu, K. O'Brien, Y.-H. Zhang, H. Yu, H. Jiang, *Appl. Phys. Lett.* **2010**, *96*, 041111.
[52] J. W. Goodman, *Introduction to Fourier Optics*, Roberts and Company Publishers, Greenwood Village, CO **2005**.
[53] B. Voisiat, W. Wang, M. Holzhey, A. F. Lasagni, *Sci. Rep.* **2019**, *9*, 7801.